Simulation approach and scale effects for sail-driven cargo ships in sideslip

Jeroen Wackers, Gaétan Rousseau, Ganbo Deng

Simulation approach and scale effects for sail-driven cargo ships in sideslip

Jeroen Wackers*, Gaétan Rousseau*†, and Ganbo Deng*
*LHEEA Lab – Centrale Nantes/CNRS, † GMP, IUT de Nantes
jeroen.wackers@ec-nantes.fr

1 Introduction

With the need to reduce carbon emissions in shipping, wind-assisted or fully sail-driven cargo transport is a major subject for naval architecture in the coming years. This requires research on CFD analysis for these ships. The pioneering work of Van der Kolk (2020) shows that, hydrodynamically, sailing hulls operate in sideslip conditions to counteract the lateral force of the sails, so sideslip is no longer restricted to manoeuvring, but has to be considered for the optimisation of calm-water resistance.

This paper considers if common CFD practices for calm-water resistance and local flow simulation can be used for sail-driven cargo ships. Specifically: (1) are the numerical setup protocols that were developed for straight-ahead sailing, valid for moderate sideslip? And (2), do the same scaling rules from model scale (MS) to ship size (FS) apply? These points are tested on a Series 60 $C_b = 0.6$ hull, which has earlier been studied by Queutey and Visonneau (2007).

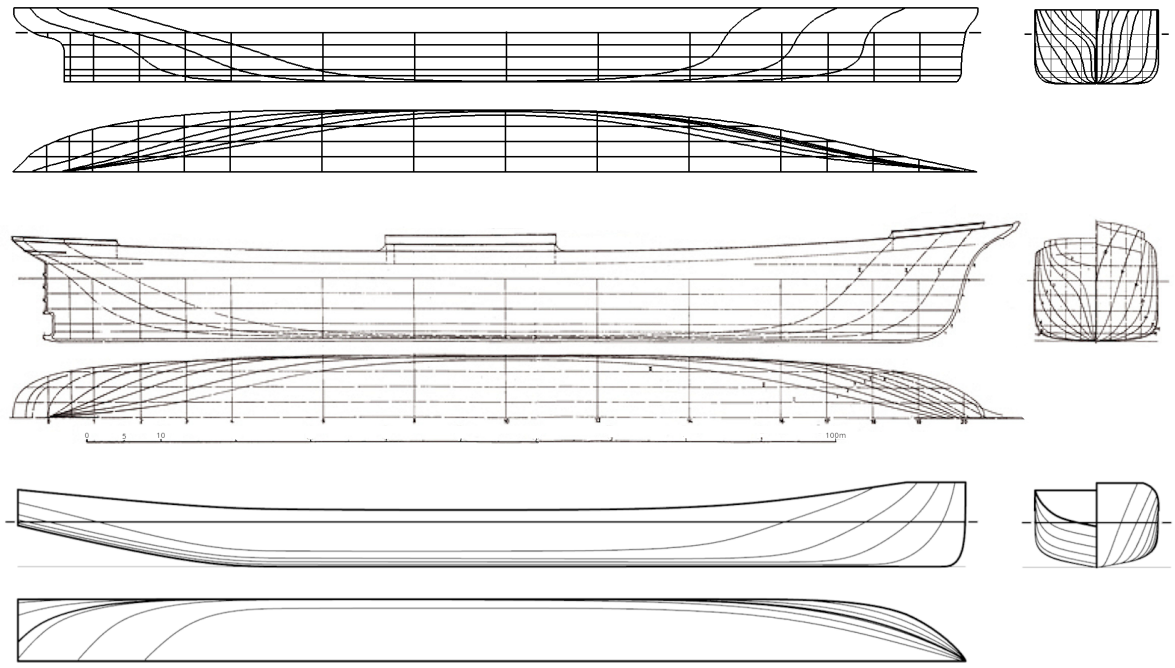

Fig. 1: Line plan of the Series 60 $C_b = 0.6$ (top), the 5-mast full-rigged bulk carrier *Preußen* (middle), and the DWA hull #34 from Van der Kolk (2020) (bottom).

2 Test case

Finding the right case The best example of modern sailing cargo hulls in the open literature is probably the DWA series (Van der Kolk (2020)). However, the tests in the current paper require high-quality local flow data, which are not available for the DWA series and, indeed, hard to find in general. The Series 60 $C_b = 0.6$ ship (Todd (1963)) is motor-driven, but it closely resembles the sailing cargo hulls of the 19th and early 20th century. Apart from the sharper bow, its lines are close to the bulk carrier *Preußen* (figure 1). In terms of size, proportions, and performance (table 1), the similarity with *Preußen* and the famous tea clipper *Cutty Sark* is confirmed, while modern ships are close enough (although these tend to have smaller drafts, flatter transom sterns, and more prudent cruising speeds than their predecessors).

Table 1: Characteristics of the Series 60 $C_b = 0.6$ hull compared with different sailing cargo vessels.

	L_{wl} [m]	L/B	L/D	C_b	$V_{\max}$ [kts]	$Fr_{\max}$
Cutty Sark (1869)	64.8	5.90	10.12	0.62	17.5	0.357
Preußen (1902)	122.0	7.44	14.77	0.67	20.0	0.297
Series 60 $C_b = 0.6$ (1951)	121.9	7.50	18.75	0.60	21.3	0.316
DWA hull #34 (2020)	138.0	7.67	21.28	0.64	15.0	0.210
Neoliner (2025)	136.0	5.67	24.73	0.60	11.0	0.155

Regarding suitable sideslip angles β for the tests, the capacity to sail upwind is determined by the ratio of sideforce to drag C_S/C_T, which in the experiments by Longo and Stern (2002) is highest at $\beta = 10^{\circ}$. However, high sideslip angles carry a significant drag penalty, so cargo ships are likely to choose routes which limit the amount of upwind sailing. A ratio $C_S/C_T = 1$, which corresponds to beam reaching, is obtained for β around 3°. Thus, $\beta = 10^{\circ}$ cannot be excluded but $\beta \leq 5^{\circ}$ in most operational conditions.

Test case definition The test is based on the experimental setup of Longo and Stern (2002). For the reasons stated above, the sideslip angles are $\beta = 0^{\circ}$ to 10°. Froude and Reynolds numbers are $Fr = 0.16$ ($Re_{MS} = 2.68 \cdot 10^6$, $Re_{FS} = 5.68 \cdot 10^8$) and $Fr = 0.316$ ($Re_{MS} = 5.30 \cdot 10^6$, $Re_{FS} = 1.12 \cdot 10^9$). The model scale is $1:40$. The hull is fixed, in the experimentally measured attitude for the model-scale force tests and in the design position for the local flow and scale effect studies.

Reynolds-averaged Navier-Stokes (RANS) equations are solved with the anisotropic EASM turbulence model (Duvigneau et al. (2003)) and a wall law with first-cell thickness $y^+ = 60$ for MS and $y^+ = 300$ for FS. The computational domain runs from $1L_{pp}$ in front of the bow to $2.5L_{pp}$ behind it, sideways to $\pm 2L_{pp}$, and vertically from $1.5L_{pp}$ below the waterline to $0.5L_{pp}$ above it. Far-field (velocity) conditions are prescribed on the lateral domain faces, with imposed pressure on the top and bottom. Sideslip angles are imposed by rotating the entire domain and forces are given in body-aligned coordinates. With the wetted area $S = 2526.4m^2$ in FS and $1.579m^2$ in MS, the force coefficients are:

$$C_T = F_x/(\tfrac{1}{2}\rho U_\infty^2 S), \qquad C_S = F_y/(\tfrac{1}{2}\rho U_\infty^2 S). \tag{1}$$

3 Flow solver and numerical setup

Solver The unsteady finite-volume Navier-Stokes solver ISIS-CFD is developed by Centrale Nantes / CNRS and distributed by Cadence Design Systems as part of FINE/Marine, which also contains the mesher Hexpress. ISIS-CFD features a mixture-fluid formulation to model the water-air interface (Queutey and Visonneau (2007)), various RANS and hybrid RANS/LES turbulence models, 6-DoF resolved or imposed body motion, and mesh deformation or overset meshing to handle moving bodies.

Adaptive grid refinement (Wackers et al. (2022)) allows the mesh to be automatically refined locally, during the computation, according to the needs of the flow. The mesh is adapted by anisotropic local division of the cells, based on a metric-tensor refinement criterion which is a real-valued tensor field computed from the flow. The mesh is refined until the mesh size times the criterion is equal to a constant threshold T_r throughout the mesh. Varying this T_r allows the mesh size to be adjusted globally.

Calm-water resistance protocol Wackers et al. (2022) define a standardised simulation setup protocol based on mesh adaptation for the resistance of bare-hull displacement ships. This protocol provides consistent, reliable simulations, since the adaptation ensures that all flow features are captured. Furthermore, results were shown to be more accurate than on non-adapted meshes, for the same numbers of cells.

The mesh adaptation in the protocol is based on combined free-surface adaptation (threshold $T_{rS} = 1.3L_{pp}/1000$) and refinement based on the second derivatives of pressure and velocity (threshold $T_{rH} \in [0.2L_{pp}, 0.025L_{pp}]$ for coarse to fine meshes). Cells smaller than $L_{pp}/1000$ are no longer refined and horizontal refinement is suppressed from $0.3L_{pp}$ behind the stern. The initial mesh is kept coarse, with cubic cells of $L_{pp}/128$ on the hull and no initial free-surface refinement. The time step is chosen such that the ship passes its own length in $100\Delta t$, and it is accelerated from rest in the first 100 time steps.

4 Grid convergence and applicability of the protocol

First, the numerical uncertainty and correspondence with measurements are evaluated in model scale. For this, each condition is simulated with a series of 5 meshes using thresholds T_{rH} from $0.2L_{pp}$ to $0.05L_{pp}$. Depending on β and Fr, the meshes have $320k$–$1.1M$ cells ($T_{rH} = 0.2L$), $490k$–$1.6M$ ($T_{rH} = 0.14L$), $880k$–$2.4M$ ($T_{rH} = 0.1L$), $1.7M$–$4.0M$ ($T_{rH} = 0.07L$), and $2.9M$–$6.4M$ ($T_{rH} = 0.05L$).

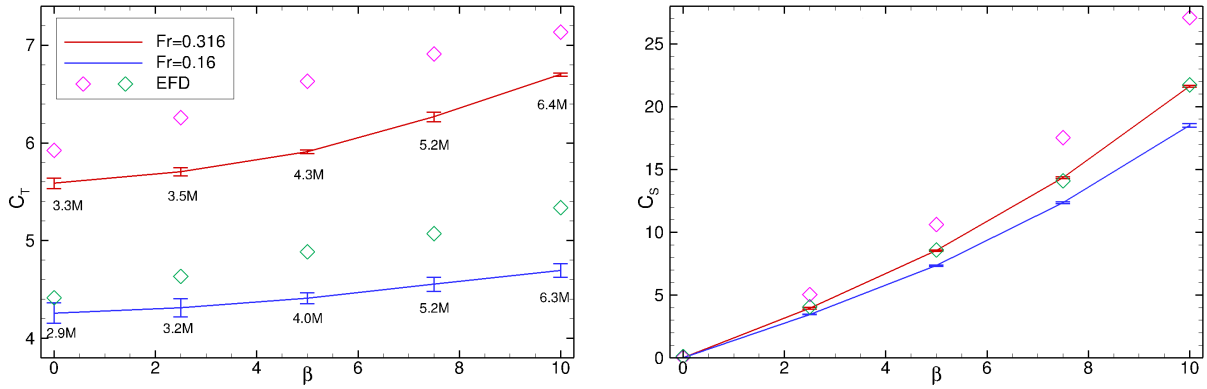

Fig. 2: Model-scale resistance (left) and sideforce (right) at $T_{rH} = 0.05L$ as a function of the sideslip angle, with numerical uncertainty, experiments, and numbers of cells.

Forces Figure 2 shows the resistance and side force as a function of β, compared with the measurements of Longo and Stern (2002) and with numerical uncertainty estimations based on the 2023 version of the Eça & Hoekstra approach (Eça et al. (2023)). The uncertainty for C_T on the finest meshes ($T_{rH} = 0.05L$) is 1–2% for $Fr = 0.316$ and 3–5% for $Fr = 0.16$, while for C_S it is always below 1%. The uncertainty shows no systematic increase with β; the variations are caused by the strong reaction of the estimation to small fluctuations in the data, since the difference between coarse- and fine-mesh solutions (not shown) is similar for all β. However, the mesh size increases with sideslip: the adaptive refinement detects that the flows become more complex and increases the number of cells to conserve numerical accuracy.

Given estimated experimental uncertainties below 1% Longo and Stern (2002), the difference between simulations and experiments is dominated by modelling error. For the resistance, the small-size model required a transition stimulator of 10×3.2 mm studs at 9.5 mm intervals to obtain the desired boundary layer behaviour. These studs, which are not simulated, probably add at least 10% to the experimental resistance. For the sideforce, the propeller axis and hub (which are absent from the CAD model) could explain part of the difference. However, the difficulties in predicting separated flows, discussed below, doubtlessly contribute to the modelling error.

Local flow Figure 3 shows the model-scale wave field for $Fr = 0.316$, comparing coarse and fine grids. At $\beta = 0^o$ the agreement between simulations, and with the experiments, is exceptional: all lines nearly overlap. At $\beta = 5^o$ the agreement between the simulations remains the same, while for $\beta = 10^o$ it is locally degraded around the bow wave. This is due to the strong breaking wave, which is sensible to the grid size: for $Fr = 0.16$ and $\beta = 10^o$ where no breaking occurs, the agreement is as good as for $\beta = 0^o$, considering the very small amplitude of the waves. The correspondence with the experiments behaves the same way, showing that the wave physics are well represented for all β.

For the wake (figure 4 shows $Fr = 0.316$), the numerical accuracy is again similar for different β. However, the flow varies strongly with the sideslip. At $\beta = 0^o$, the wake is essentially a flat-plate flow, which is perfectly simulated except for the missing propeller hub which can be seen in the experiments. For $\beta = 10^o$, at $x/L = 0.1$ the main vortex is well captured but the leeward boundary layer near the free surface has a bulge which is too low. This bulge is related with a complex separation bubble at the bow, involving vortex separation with a Froude-dependent topology, and ventilation at $Fr = 0.16$ (figure 5). Further back, the features of the open-type separation at the stern are all represented, but not perfectly captured. This illustrates the increased complexity of the flow, compared with $\beta = 0^o$.

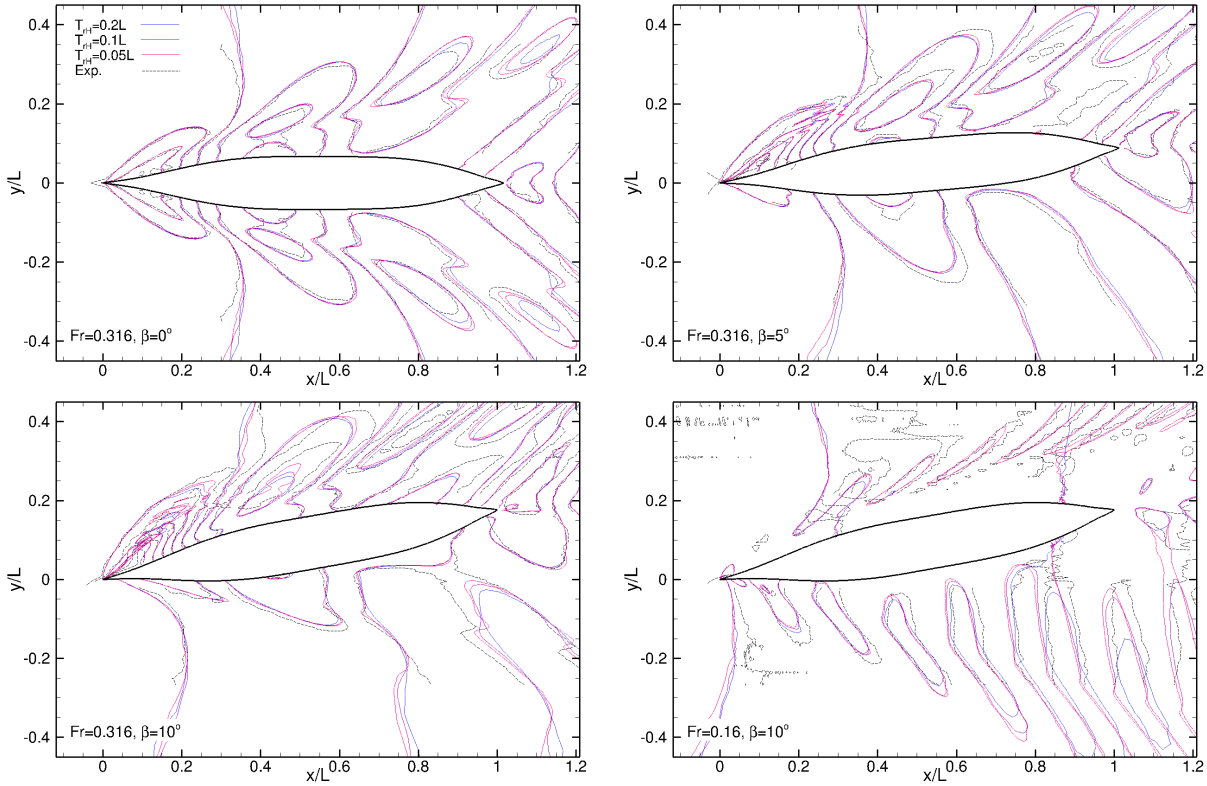

Fig. 3: Grid convergence and experiments for the wave field, as a function of β and Fr. Model scale.

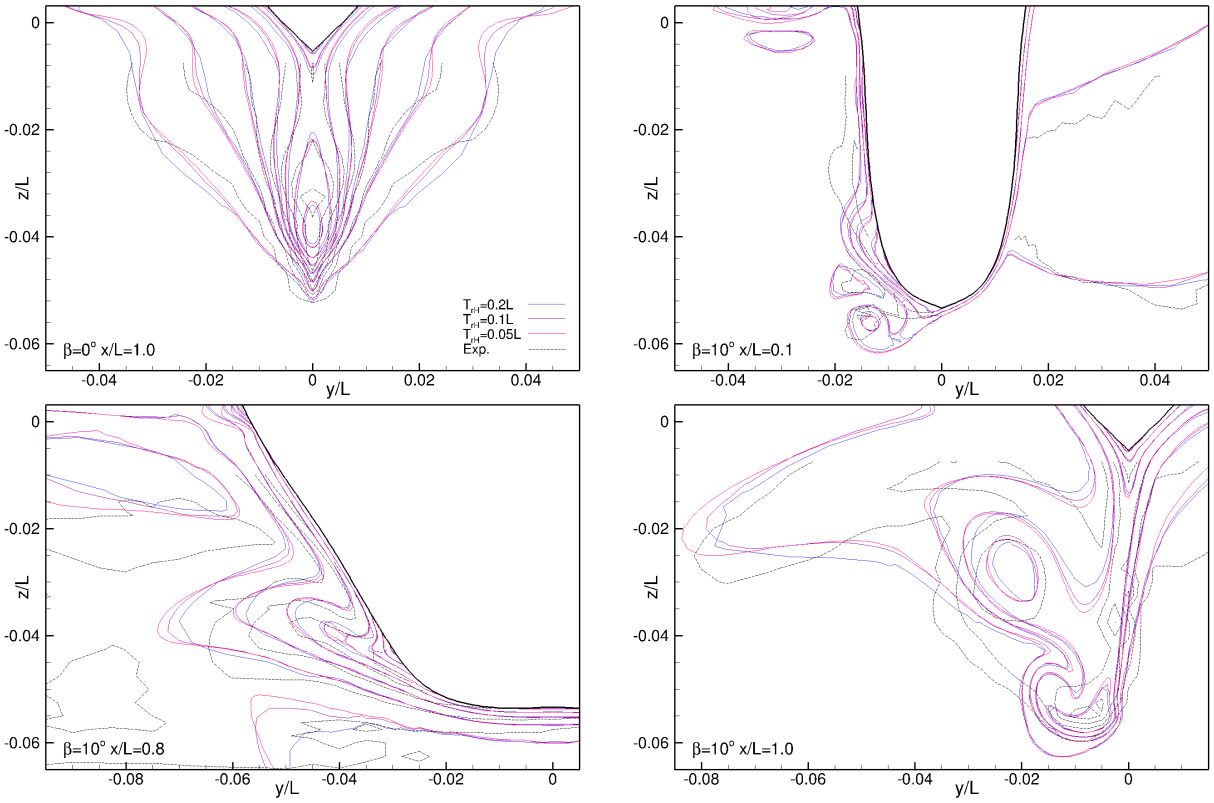

Fig. 4: Grid convergence and experiments for the axial flow in x-constant planes (body frame). Model scale, $Fr = 0.316$.

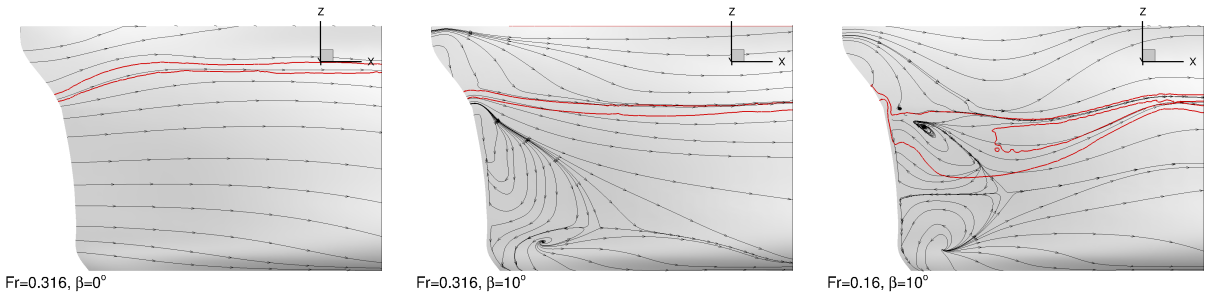

Fig. 5: Streamlines and water volume fractions 0.1 / 0.9 (red) on the leeward (port) bow. Model scale.

5 Scale effects

Figure 6 presents full-scale forces and compares them with standard extrapolations from model scale. The MS resistance is corrected following ITTC (2021) with the ITTC-1957 friction line and a form factor estimated with Prohaska's method based on $Fr = 0.16$ and 0.316. C_S is considered the same in MS and FS. The MS-based estimations are remarkably accurate, with errors close to the numerical uncertainty, and hardly degrade for increasing β. The full-scale numerical uncertainty is comparable to MS and the adapted meshes are larger than for MS, but the number of cells remains reasonable.

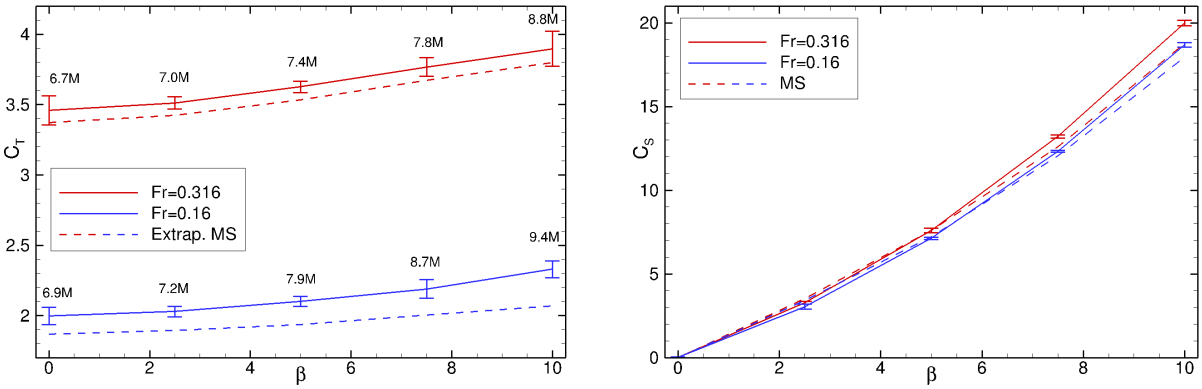

Fig. 6: FS resistance and extrapolated MS (left), FS and MS sideforce (right), $T_{rH} = 0.05L$.

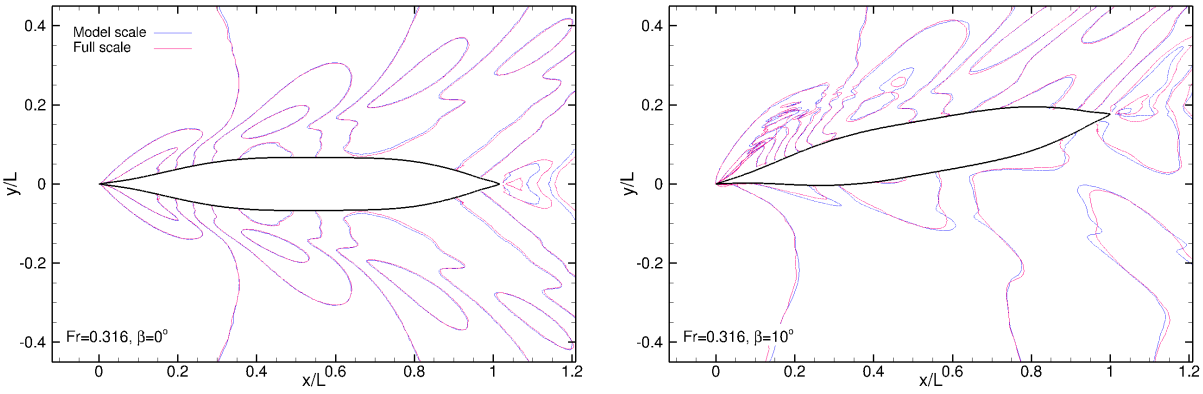

Fig. 7: Scale dependence of the wave field for $Fr = 0.316$.

Froude's hypothesis is also confirmed for the wave field (figure 7), which only shows small differences near the stern. For the wake (figure 8) the scale effect at $\beta = 0^o$ is only a reduction of the boundary-layer thickness. However, it is more complex in sideslip. The velocity defect is reduced, and confined to a smaller region, but the main vortical structures remain in place. Thus, the wake is a mixture of *Re*-independent vorticity, induced by the sideward lift created by the sideslip, and scale-dependent wake flow, which is hard to extrapolate between model and full scale.

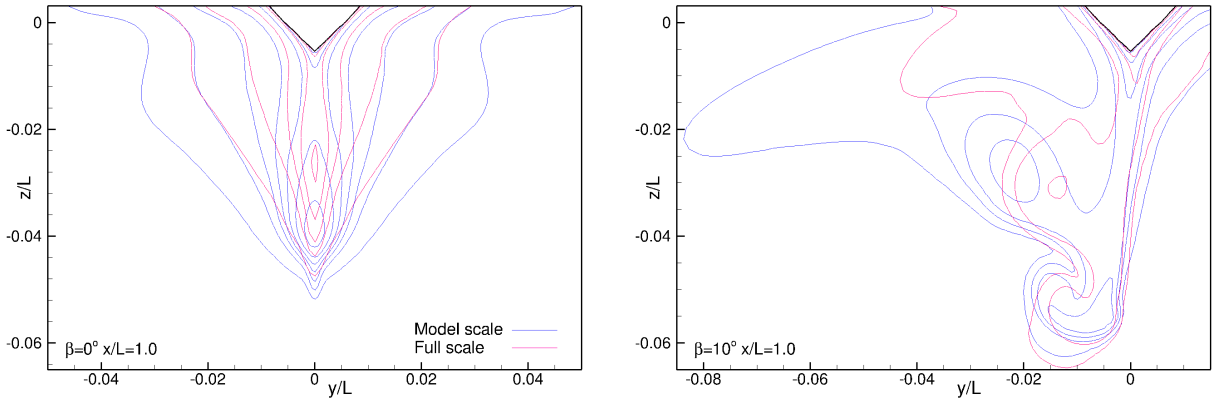

Fig. 8: Scale dependence of the wake at $x/L = 1.0$, $Fr = 0.316$.

6 Conclusions

The tests show that, thanks to the adaptive meshing, the numerical uncertainty has little dependence on β, which implies that our standard numerical protocols apply to sailing cargo ships. However, flows with sideslip exhibit complex physics, which may require more sophisticated modelling than RANS with wall laws. Extrapolation from MS to FS (and by inference, using model tests for design) appears valid for the forces and the wave fields. However, accurately representing the wake, which is crucial for the design of appendices, and propellers of wind-assisted ships, requires FS simulation.

These findings are preliminary, and have to be confirmed by more extensive studies, considering for example modern transom-stern hulls. Accurate local-flow measurements for such hulls in sideslip conditions would be very helpful.

Acknowledgements

We thank Prof. Frederick Stern for providing the Series 60 experimental data and Dr. Luis Eça and Dr. Serge Toxopeus for their help with the uncertainty estimation.

References

R. Duvigneau, M. Visonneau, and G.B. Deng (2003). On the role played by turbulence closures in hull shape optimization at model and full scale. *J. Mar. Sci. Tech.*, **8**(1), 1–25.

L. Eça, S.L. Toxopeus, and M. Kerkvliet. *Procedures for the estimation of numerical uncertainties in the simulation of steady and unsteady flows*. IST Report IST-M 8, Lisbon, Portugal. See also https://www.marin.nl/en/research/free-resources/verification-and-validation

International Towing Tank Committee (2021). *Resistance Tests*. ITTC Procedure 7.5-02-02-01.

N. van der Kolk (2020). *Sailing Efficiency and Course Keeping Ability of Wind Assisted Ships.* Ph.D. thesis, Delft University of Technology.

J. Longo and F. Stern (2002). Effects of drift angle on model ship flow. *Exp. Fluids*, **32**, 558–569.

P. Queutey and M. Visonneau (2007). An interface capturing method for free-surface hydrodynamic flows. *Comput. Fluids*, **36**(9), 1481–1510.

F.H. Todd (1963). *Series 60. Methodical experiments with models of single-screw merchant ships*. David Taylor Model Basin, report 1712.

J. Wackers, G.B. Deng, C. Raymond, E. Guilmineau, A. Leroyer, P. Queutey, and M. Visonneau (2022). Adaptive grid refinement for ship resistance computations. *Ocean Eng.*, **250**, 110969.